

# Development and field tests of a narrowband all-reflective spatial heterodyne spectrometer

J. B. CORLISS,<sup>1,\*</sup> W. M. HARRIS,<sup>1</sup> E. J. MIERKIEWICZ,<sup>2</sup> AND F. L. ROESLER<sup>3</sup>

<sup>1</sup>Lunar and Planetary Laboratory, University of Arizona, Tucson, Arizona 85271, USA

<sup>2</sup>Embry-Riddle Aeronautical University, 600 S Clyde Morris Blvd., Daytona Beach, Florida 32114, USA

<sup>3</sup>Department of Physics, University of Wisconsin-Madison, Madison, Wisconsin 53706, USA

\*Corresponding author: corliss@lpl.arizona.edu

Received 9 July 2015; revised 9 September 2015; accepted 15 September 2015; posted 15 September 2015 (Doc. ID 245666); published 12 October 2015

We describe the design, development, and performance of a narrowband, all-reflective, unaliased spatial heterodyne spectrometer (SHS) that has been tested in observations at the focus of the 1.6 m main telescope of the McMath–Pierce solar telescope on Kitt Peak. The all-reflective SHS described herein is a highly robust common-path Fourier transform spectrometer without moving parts that, over a limited spectral region, combines the large field of view and high resolving power characteristic of interference spectrometers but at substantially reduced instrument size and optical tolerances. The self-scanned region of wavelength space and resolving power of the SHS are determined by the beam size, the diffraction grating groove density, the number of detector elements, and the fixed orientation of a set of pilot mirrors. The results presented here represent the first successful implementation of this reflective SHS design for field use. We discuss concepts behind the unaliased reflective SHS design and report the performance of the instrument when used to observe terrestrial airglow and absorption features, the solar spectrum, and the Jovian spectrum near  $\lambda = 6300 \text{ \AA}$ , at the achieved resolving power ( $R = \lambda/\delta\lambda$ ) of  $R > 100,000$ . The results confirm that reflective SHS instruments can deliver effective interferometric performance in the visible to the far-ultraviolet wavelengths with commercial optics of moderate surface quality. © 2015 Optical Society of America

**OCIS codes:** (300.0300) Spectroscopy; (300.6320) Spectroscopy, high-resolution; (300.6300) Spectroscopy, Fourier transforms; (220.0220) Optical design and fabrication.

<http://dx.doi.org/10.1364/AO.54.008835>

## 1. INTRODUCTION

High-resolution spectroscopy (HRS) has proved crucial in many fields of scientific study by providing greatly increased sensitivity to Doppler shifts, line shapes, emission/absorption feature separation, and identification. This has enabled the study of the energetic universe, including shocks, dynamical structures, and complex radiative and absorptive processes, albeit with technical limitations that restrict its use for certain targets. However, the most common instrument used for high resolving power, the cross dispersed echelle spectrometer (DES), relies on a very small field of view (FOV) to reduce the size of the aperture image relative to the dispersion relation in the imaged spectrum. Because of this, DES instruments are typically used at large aperture telescopes where collecting area can recover the étendue ( $=A_{\text{eff}} \times \text{FOV}$ ) lost with the smaller aperture. As a result there is an instrumental gap for HRS of angularly extended targets and for observations at smaller diameter telescopes where observing time is more abundant. Our goal in the project reported here was to develop a powerful

and versatile HRS instrument with superior characteristics for wide-field study of the energetic universe and to field test this instrument through observations of terrestrial and astronomical objects with complex spectral structure.

One solution for providing high spectral resolution without the FOV limitation of DES is to employ an interferometric instrument such as a Fabry–Perot interferometer or a scanning Fourier transform spectrometer (FTS) (e.g., [1]). These instruments can support a large FOV at high resolving power, thus delivering large intrinsic étendue. This gives FTS instruments an inherent advantage for observations of angularly extended targets and permits their use with smaller aperture telescopes and in resource-limited environments like planetary probes. Such technologies have proven useful for the study of faint extended emission sources, but they also come with very tight restrictions on the surface quality, thermal uniformity, and the positioning of the optical components that become increasingly difficult to manage toward shorter wavelengths. In vacuum ultraviolet (VUV), the use of etalons, beam splitters, and other

transmitting elements becomes a limiting factor, and short of the transmission cutoff of LiF near  $\lambda = 1000 \text{ \AA}$  they cannot be used at all.

To address the limitations imposed by conventional interferometer designs, we have designed, constructed, and validated a variation, first suggested by Harlander [2], of an unaliased all-reflective, common-path spatial heterodyne spectrometer (ARC-SHS from here on) that has much less restrictive tolerances than conventional interference spectrometers while still delivering their advantages [2–5]. SHS instruments are two-beam interferometers configured similarly to conventional designs such as a Michelson or Sagnac, but, by replacing the mirrors of the Michelson or the beam splitter of the Sagnac with diffraction gratings, a SHS *simultaneously* captures its entire bandpass at high resolving power and *without* moving parts (self-scanning). The particular ARC-SHS described in Section 2 delivers 140 times the étendue of the McMath–Pierce stellar spectrograph in <1% the volume, at a comparable resolving power. In addition to the advantages inherited from the conventional SHS designs, further benefits particular to the ARC-SHS family discussed herein are (a) common path: much more forgiving in its alignment and stability; (b) all-reflective: effective use under  $\lambda = 1100 \text{ \AA}$  and immune to the wavelength dependency in optical power of transmitting optics; and (c) the use of a single grating as both beam splitter and combiner: alleviates fringe quality degradation from key optical surfaces.

## 2. INSTRUMENT

### A. Basic Design and Performance

The single-order, narrowband ARC-SHS described here was initially constructed as a prototype for a VUV sounding rocket experiment that has since flown to observe emissions in the interplanetary medium ([6,7]). Extensive and successful laboratory tests of this general design between 200–7000  $\text{\AA}$  paved the way for other instrumental systems of similar configuration [8,9] and led to a field-ready instrument for studies of terrestrial and astronomical sources near  $\lambda = 6300 \text{ \AA}$ . Here and in the sections that follow we describe the specifics of the all-reflective design and the field-ready, high-spectral-resolution ( $R > 100,000$ ), unaliased bench-top instrument that was installed and operated at the focus of the 1.6 m main telescope of the McMath–Pierce facilities at Kitt Peak. We will discuss the theoretical and realized characteristics of the instrument and results from its successful operation observing targets of different angular extent and with intrinsic brightness variation of more than three orders of magnitude.

The ARC-SHS itself consists only of three optical components: the grating, a right angle roof mirror, and an optical flat mirror (Fig. 1). In the basic configuration, collimated light enters the interferometer and strikes the upper half of a symmetrically ruled grating at normal incidence, where it is split into two beams (orders  $\pm m$ ) that countercirculate through the interferometer via a common series of pilot mirrors (Fig. 1). After diffraction, the roof-pilot mirror translates each beam perpendicular to the dispersion plane, preventing overlap between the input and output. The countercirculating beams produce a virtual image of linear fringes at a fringe localization plane (FLP) near the midpoint of the optical path. The fringes

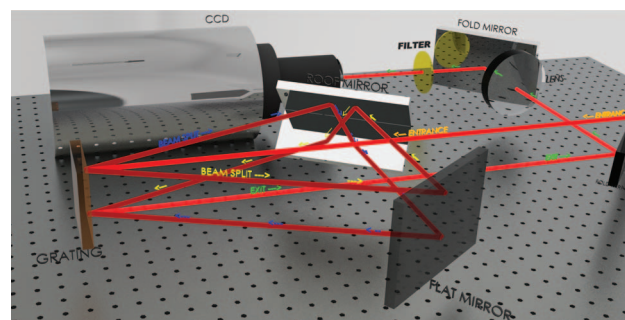


**Fig. 1.** Zemax ray trace and three-dimensional (3D) model (to scale) of optical breadboard layout (1" square bolt hole pattern).

result from an accumulating optical path difference (OPD) between the wavefronts of the two counter-rotated beams. This crossing angle ( $\gamma$ ), along with the resulting frequency–wavelength relationship, is set through rotation of the pilot mirrors such that, for a selected grating dispersion angle (or wavelength), the two wavefronts are in phase ( $\gamma = 0$ , Appendix A). After passing through the FLP, the returning beams recombine at an isolated location on the grating where the antisymmetric orders diffract a second time and exit the interferometer parallel to the entering beam. A mirror or lens then focuses and magnifies the interference pattern onto a charge coupled device (CCD) detector. The width ( $W$ ) of the input beam on the grating is proportional to the resolving power of the instrument following relationship  $R = 4 mW/d$ , where  $d$  is the groove spacing and  $m$  is the order of diffraction. Each fringe frequency in the interference pattern represents a spectral feature with a separation from the heterodyne condition, a predetermined central wavelength  $\lambda_0$  where  $\gamma = 0$ , with each discrete fringe frequency corresponding to an integer number of resolution elements ( $d\lambda$ ). The number of frequencies, and the resulting instrument bandpass that can be detected, is limited by the number of detector pixels in the fringe plane [2]. Wavelengths beyond this limit are avoided for the reasons that are common in Fourier transform signal processing and frequency discrimination (see below). A narrowband interference filter is commonly used to prevent out-of-band light from reaching the detector. The instrumental étendue is the product of the illuminated area of the grating and the FOV ( $\Omega \sim 2\pi/R$ ) of the source. The étendue is limited by the acceptable range of incident field angles diffracted at the grating, which results in some spectral broadening and loss of power in spectral features contributing from the edges of the FOV for an aperture-filling source. A practical limit to  $\Omega$  is reached when the broadening approaches the resolving power of the instrument.

Spectral information from the incoming beam is obtained by taking a Fourier transform of the interference pattern produced in the ARC-SHS. The most significant systematic limiting factors affecting the quality of the transformed spectrum are multiplexing noise, spectral aliasing, apodization of the interference pattern, and internal optical path difference disruptions (OPDD) in the circulating optics (Appendix A). Aliasing of symmetric fringe frequencies with equal but opposite wavefront rotations ( $\pm\gamma/2$ ) relative to the heterodyne condition

( $\gamma = 0$ ) is a fundamental concern of all SHS devices, but it is eliminated in the ARC-SHS with the roof mirror and a symmetry-breaking rotation ( $\phi$ ) of the “pilot-flat” mirror in the plane perpendicular to dispersion (Appendix A). The resulting interference pattern produced in the ARC-SHS is related to OPD from both the crossing angles  $\gamma$  and  $\phi$  between the wavefronts. In general the uniformity of the wavefronts is affected by the surface uniformity of each optical surface, which can disrupt the OPD and thus affect the fringe formation location(s) (i.e., fringe distortion). However, the ARC-SHS is significantly less sensitive to this effect because interfering ray pairs are produced from the same point on the grating; thus the OPDD accumulations due to uniformity variations at the grating interface are relieved (Appendix A). As a result, the ARC-SHS is extremely forgiving of these surface imperfections. Further, the common path nature of the system provides a very robust design. The OPD is immune to pure translations (pilot mirrors and the grating), and the system is also immune to any “roll” in the roof-pilot mirror. For a given heterodyne tune-in angle, the system is automatically set to a zero path. Hence, the alignment is forgiving, and tuning the instrument is relatively uncomplicated. All these features become increasingly useful for shorter wavelength applications, where tolerances are typically proportional to the wavelength. Other tolerances (e.g., mirror/grating rotations) are comparable to other SHS designs described in previous reports (e.g., [2]).

## B. Field Version

Successful laboratory tests of the ARC-SHS (under NASA grant NAG5-12812) were made at wavelengths from  $\lambda \approx 1900$ –7000 Å and led to the development of a field version that was successfully incorporated into the fixed focal plane of the 1.52 m,  $f/54$  main telescope of the McMath–Pierce Solar Observatory on Kitt Peak, providing a unique tool for cometary emission line studies [10]. The instrument itself was assembled as a prototype for a VUV flight experiment (NASA grant NNG05WC22G, [6]). Figure 2 shows a CAD model of the optical setup along with the actual instrument during testing at Kitt Peak. Coupling to the McMath–Pierce telescope included four additional optical elements. A dichroic was inserted into the converging beam from the McMath–Pierce to direct the blue end of the visible spectrum to a guide camera–Fresnel lens combination that was used for object tracking. A lens was

also inserted downstream of the dichroic to adjust the  $f/\#$  of the telescope beam to match the  $f/\#$  of the ARC-SHS in order to optimize the étendue. A field lens (L2) was inserted close to the telescope focus that images the primary mirror onto the FLP, which has the effect of creating a pupil at the FLP for filling the off-axis FOV field vectors within the imaged interferogram. A third lens was then used to collimate the beam at the ARC-SHS entrance. The use of transmitting optics in the input and output optics was done to facilitate the rapid setup of the instrument and could be replaced with off-axis mirrors to make the system fully reflective if desired [11].

The input to the ARC-SHS was a collimated 35 mm high and 75 mm wide (W) beam illuminating a 600 groove/mm holographic diffraction grating that dispersed the light into two first-order ( $m = \pm 1$ ) beams (Fig. 1). The theoretical resolving power was  $R = 4W/\sigma \sin \theta = 4mW/d = 4 \times 75 \times 600 = 180,000$ , with the difference between two adjacent fringe frequencies equal to the heterodyne wavelength divided by  $R$  ( $d\lambda = \lambda_o/R$ ). This dictated the maximum input acceptance angle ( $\Omega_{\max} = 3.5 \times 10^{-5}$  sr) and hence the optimized  $\text{FOV}_{\text{opt}} = (0.075/D_T)^2 \times \Omega$ , where  $D_T = 1.52$  m, the diameter of the McMath–Pierce main telescope. The interferometer could be manually tuned from  $\lambda \approx 5000$  to  $\approx 7500$  Å while maintaining the resolving power by rotating the pilot mirrors, with the limit coming from the projected widths of the individual surfaces in the direction of each beam. The instrument was aligned for a heterodyne condition near the wavelength of the metastable  $^1D$  line of OI at  $\lambda_o \approx 6300.3$  Å, with a corresponding theoretical  $d\lambda = 0.035$  Å. Following the Nyquist criterion, the limiting bandpass ( $\delta\lambda$ ) of the instrument is half the sampled pixels in each fringe formation direction multiplied by the spectral width of the resolution element ( $d\lambda$ ); the fringe counter-rotation (unaliasing) and the use of a single order of diffraction provides two fringe formation directions or a sampled bandpass  $\delta\lambda = 2 \times (N_{\text{pix}}/2) \times d\lambda = 2(512/2)(0.0035) = 17.9$  Å (Appendix A). This value is less than 20% of the  $\sim \pm 100$  Å range in wavelength admitted by the optical configuration and physical size of the pilot mirrors. The out-of-band light contains unresolved fringe frequencies that can introduce aliasing beat frequencies and contribute to the multiplexing noise, thus producing unwanted information in the transformed spectrum (see above). To avoid this, a transmission filter with a  $\sim 7$  Å full width at half-maximum (FWHM) was used to limit the wavelength range reaching the detector. The filter's peak transmission of 40% at  $\lambda \approx 6300$  Å fell to 10% at the edge of the reported spectra, introducing a progressive reduction in throughput and signal/noise toward the edge of the bandpass (Fig. 6 left, Fig. 7). This effect was primarily relevant for continuum sources.

## 3. DATA REDUCTION

The data reduction pipeline used to prepare interferograms for transforming used standard CCD and FTS processing techniques including bias subtraction and application of a flat field. To prevent sharp-edge induced ringing in the Fourier transform, the interferograms were apodized with a Hanning function to taper the signal level to zero at the edges. Spatial nonuniformity in the illumination, unrelated

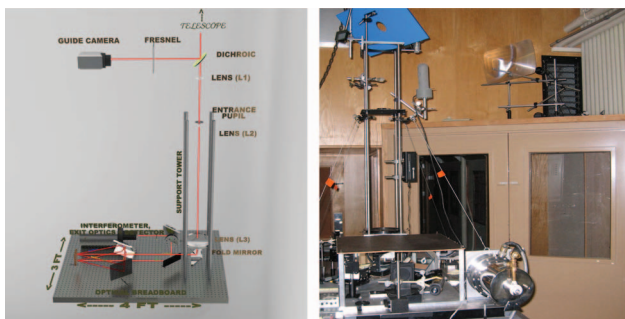


**Fig. 2.** (Left) Ray trace and 3D model of optical coupling for the McMath–Pierce. (Right) Photo of the instrument coupled to the McMath–Pierce main telescope. (Right and left are approximately mirror images of each other.)



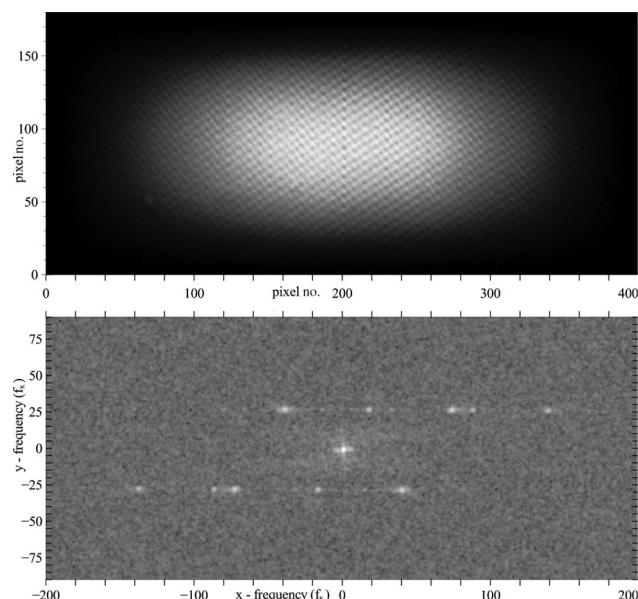


**Fig. 3.** (Top) Two-dimensional (2D) interferogram containing multiple Th-Ar calibration emission features. (Bottom) Power spectrum of the 2D Fourier transformed Th-Ar interferogram above.

to interference, was removed by co-adding noncoherent individual images of each beam of the interferometer with the opposing arm blocked, a flat-fielding method described in Englert and Harlander [12]. A series of Rb and Th-Ar test lamp exposures were used to determine the wavelength scale, the instrument line profile, and for alignment confirmation after extended observing runs (Figs. 3–5). A measure of the resolving power was obtained from the spectra of very narrow emission lines from a Thorium-Argon hollow cathode lamp (Fig. 4) and from unresolved telluric absorption and emission lines (Figs. 6 and 7). Based on these measurements we derived a dispersion relation of  $0.036 \text{ Å/pix}$  ( $d\lambda$ ) and a consistent resolving power of  $R \approx 100,000$  for the instrument, or about 60% of the theoretical limit (Figs. 3–6). The reduction in  $R$  is due primarily to off-axis light from the aperture FOV ( $\Omega$ ) and the Hanning function used to taper the signal level to zero at the edge of the interference pattern. The effects on the instrumental line profile from other contributors (e.g., alignment and optical surface imperfections) are small and were not removed from the processed data. The spectra were corrected for the interference filter profile by dividing out a normalized least-squared-fit to a “white” light source spectrum.

#### 4. RESULTS

The performance of the SHS was tested using adsorption lines from Jupiter and the day sky and emission lines from telluric night airglow features. Jupiter’s angular extent is comparable to the instrumental FOV at the focus of the McMath–Pierce main telescope. The ground-based observed solar spectrum near  $\lambda = 6300 \text{ Å}$  is complicated yet well known [13], containing pronounced solar absorption features along with several narrow atmospheric absorption features within the filter band that provided useful diagnostic features for characterizing the SHS

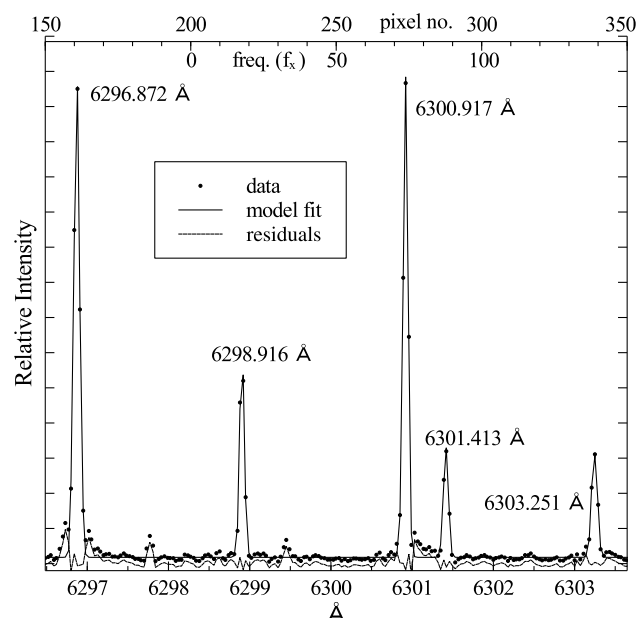


**Fig. 4.** Th-Ar hollow cathode lamp calibration spectrum produced from selected rows in the power spectrum of the Fourier transformed interferogram of Fig. 3. The least-squares best model fit provides measurements for wavelength calibration, resolving power and the instrumental profile.

wavelength scale and resolution (Fig. 6). Fits to the spectra were performed using a standard least squares fitting routine, MPFIT [14], and the results are provided in Table 1. Flux levels were corrected for the filter response as noted above; however, the impact of multiplex noise in the lowest transmission part of the profile can be seen in the post-fit residuals at the edges of the spectrum. In the measured and fitted Jovian spectrum, the solar reflected features accurately show line broadening by the 12 km/s ( $\sim 24 \text{ km/s}$  limb-limb) Jovian rotation rate and the Doppler shift of their line centers by Jupiter’s 27.2 km/s ( $0.571 \text{ Å}$ ) geocentric velocity at the time of our observations

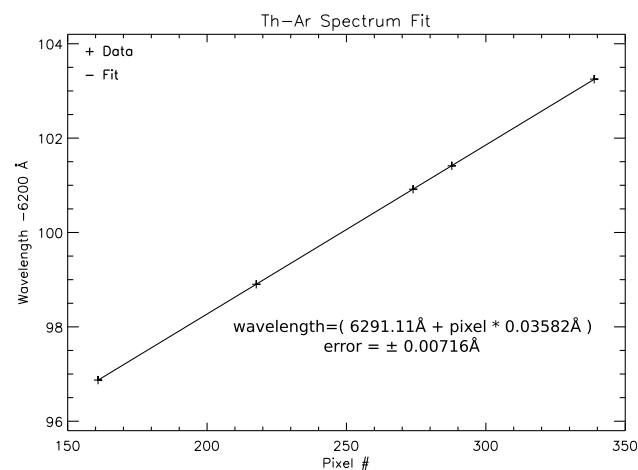


**Fig. 5.** Interactive data language (IDL) linear least squares fit to Th-Ar emission feature line centers in Fig. 4, used for calibrating the wavelength scale ( $\text{Å/pix}$  and offset).

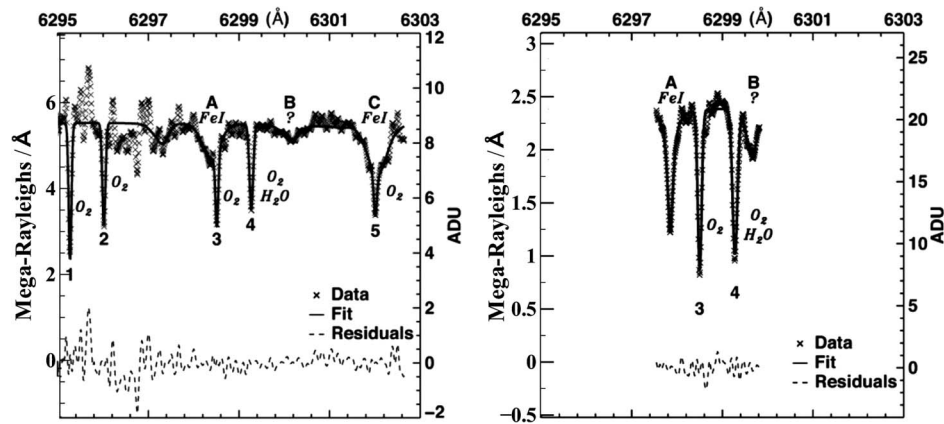


**Fig. 6.** Best fit of Jovian, telluric, and solar spectra with residuals. Line identification and reference values were taken from Moore *et al.* ([13], see also Table 1). The telluric absorption features are designated by numbers and fit with Gaussian profiles. A, B, and C correspond to pronounced solar absorption features, fit with Voigt profiles. (Left) A best fit to the spectrum of a 60 s Jupiter exposure is shown. (Right) A best fit to the spectrum of a 360 s sum of day sky exposures is shown.

(Fig. 6 left). The telluric features included lines from  $O_2$  and  $H_2O$  that were neither rotationally broadened nor Doppler shifted relative to their rest wavelengths, confirming the precision of the Jovian measurements (Fig. 6). The Jovian spectra were also compared with observations of the day sky that contained the same  $O_2$  and  $H_2O$  features as well as the unbroadened Fraunhofer features at their rest wavelengths (Fig. 6 right). Jupiter and day-sky line center measurements are compared with the standard values from Moore *et al.* [13] in Table 1. Collectively, these observations provide a detailed demonstration of the instrumental performance for resolved and unresolved lines at different wavelength separations from the tuning position. Despite decreased S/N at high fringe frequencies near the edge of the filter bandpass, all spectral features were identified to within the resolving power of the SHS and without anomalies.

The Jovian spectrum is also bright enough (5.6 MR/Å at  $\lambda = 6300$  Å, [15]) that high signal-to-noise spectra can be obtained from a short exposure, allowing characterization of the instrumental efficiency, the transmission profile of the filter, and photometric and wavelength calibration. Night sky observations of telluric airglow  $O[{}^1D]$  emission produced from the ionospheric D-layer were used to further characterize the performance and dynamic range of the instrument for an isolated unresolved emission line feature and to test stability of the alignment during long exposures. Observations obtained during the transition from daylight to a nightglow-dominated spectrum show the dynamic range of the instrument (Fig. 7).

Using Jupiter's continuum level at  $\lambda = 6300$  Å for intensity calibration, we made several measurements of  $O[{}^1D]$ , observed at similar airmass, as a test of photometric stability. Although atmospheric  $O[{}^1D]$  experiences some variation due to geophysical conditions, the nightglow values typically decrease from  $\sim 1$  kR during astronomical twilight to an asymptotic brightness of tens of Rayleighs [16,17]. Our measurements are consistent with this trend (Fig. 8). The spectra obtained show consistent throughput and fringe formation efficiency for exposures as long as 2400 s, a result consistent with high stability in the optical system.

## 5. SUMMARY

We report the successful implementation and characterization of a narrowband ARC-SHS instrument tuned near 6300 Å, at an achieved resolving power  $>100,000$ . The instrument proved exceptional performance in the field and provided powerful platform for cometary observations [10] through its combined capabilities in FOV, resolving power, spectral coverage, sensitivity, and stability. There was no sign of temporal variation in either the optical alignment or the fringe formation efficiency, as verified from calibration lamps and well-known astronomical and telluric sources on several observing runs. High precision and accurate detection of emission and absorption features of complicated spectra obtained from both faint and bright targets and of varying angular extent showed the reliability of the instrument for observing a variety of wide-field scientific targets.

**Table 1.** Measured Line Centers from Fig. 6 and Comparison to Standard Values<sup>a</sup>

Feature	1	2	3	4	5	A	B	C
Standard value	6295.178	6295.960	6298.457	6299.228	6302.000	6297.799	6299.588	6301.508
Jupiter								
Measured center	6295.175	6295.932	6298.457	6299.226	6301.998	6298.329	6300.118	6302.038
Day sky								
Measured center	X	X	6298.443	6299.231	X	6297.786	6299.610	X

<sup>a</sup>Line center values are given in angstroms and standard values are provided by More *et al.* [13].

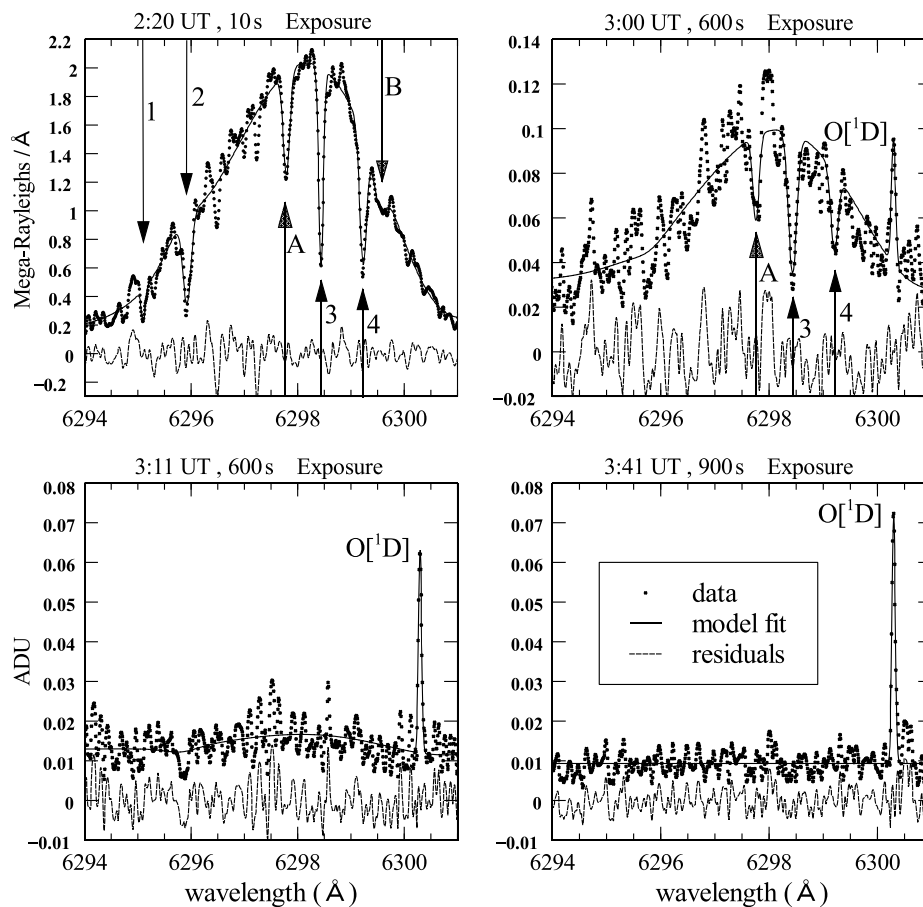


**Fig. 7.** Selected spectra examples taken through the transition from daylight into nightglow. The spectra have not been corrected for the filter profile.

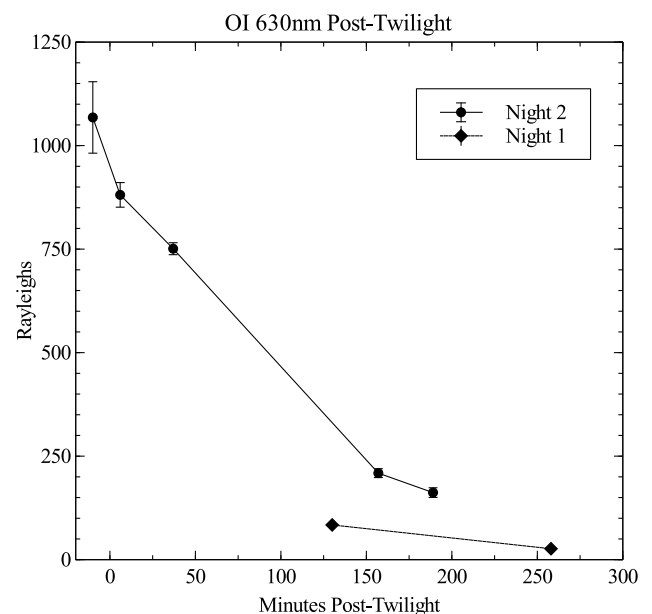
## APPENDIX A: FRINGE FORMATION, SYMMETRY, AND LINEARITY

Figure 1 shows the optical component layout to an ARC-SHS. The chromatic separation of wavefront angles are dictated in the diffraction plane by the grating equation

$$m \frac{\lambda}{d} = \sin \theta + \sin \alpha,$$

where  $m$  is the grating order,  $\alpha$  is the incident angle,  $\theta$  is the diffraction angle, and  $d$  is the physical groove spacing.

Since a particular optical path is dependent on both the diffraction angle and the rotation of the transfer mirror(s) it is possible to align a SHS so that a specific wavelength ( $\lambda_o$ ) has the recombined wavefronts parallel to one another ( $\gamma = 0$ ), producing uniform constructive interference (zero “x” frequency) at the FLP. This particular geometry is referred to as the heterodyne condition for  $\lambda_o$ . At other wavelengths ( $\lambda$ ) the wavefronts are rotated with respect to each other by a  $\gamma$  value, defined only by the grating dispersion relation. An OPD accumulates between the rotated wavefronts with increasing distance from the point where they cross (Fig. 9 top). When the value of  $\text{OPD} = n + \frac{1}{2}$  wavelengths, destructive interference occurs, while constructive interference occurs when the  $\text{OPD} = n$  wavelengths. For collimated light, normal incident



**Fig. 8.** Photometrically calibrated OI 630nm Post-Twilight measurements starting shortly after dusk. Jupiter’s continuum (5.6 MR/Å at  $\lambda = 6300$  Å) was used as the standard. The three left-most data points, going left to right, correspond to the spectra in upper right, lower left, and lower right of Fig. 7.



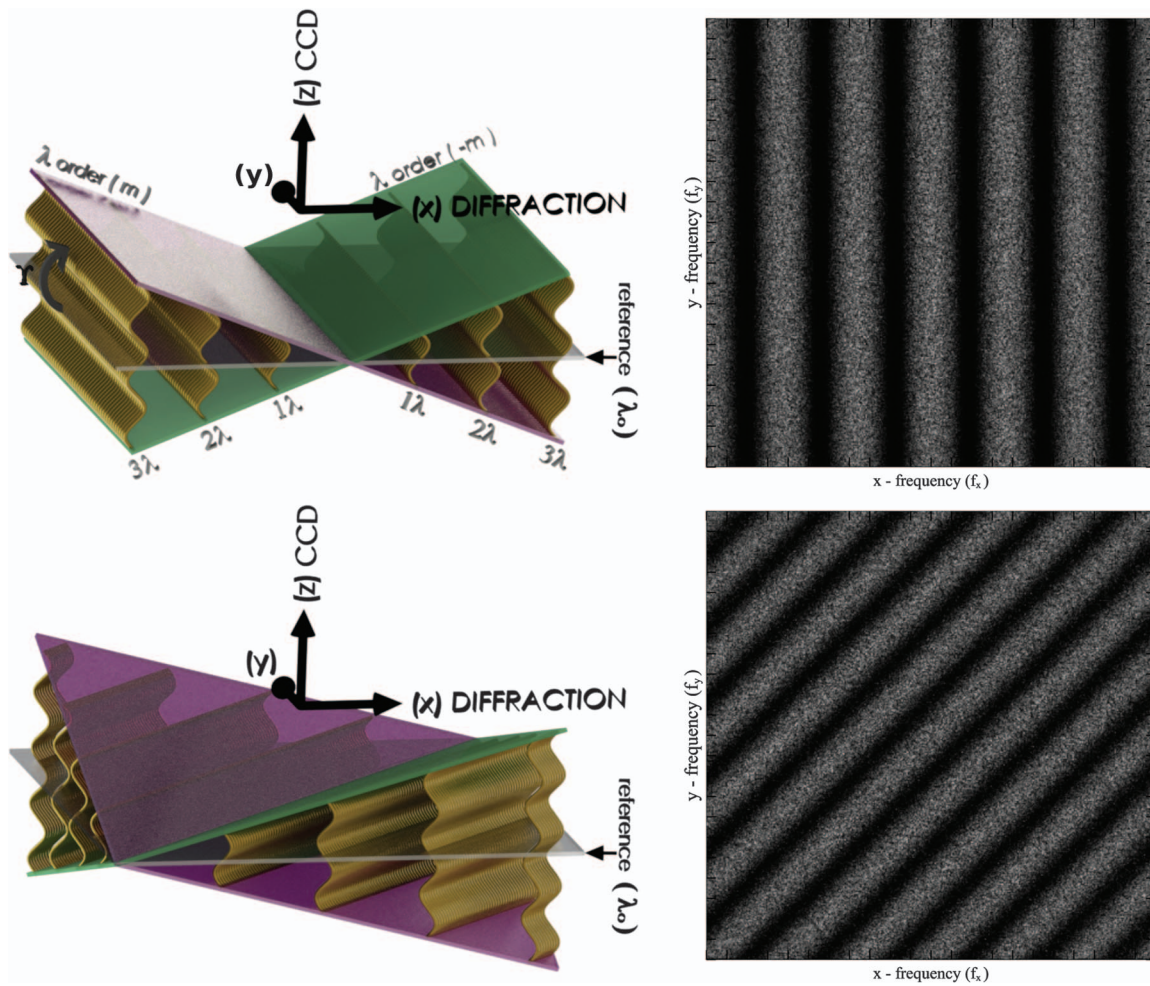


**Fig. 9.** Computer-aided design (CAD) depictions of crossing wavefront geometry and associated interferograms (produced through Zemax) for an  $x$  frequency of 6. Top: No “ $y$  tilt” produces fringes only parallel to  $y$  axis. Bottom: Positive “ $y$  tilt” produces rotated fringes with positive  $y$  frequency. Note, the  $x$  frequency remains unchanged.

on the grating ( $\alpha = 0$ ), the result is a Fizeau fringe pattern of spatial frequency that is proportional to  $|\lambda - \lambda_o|$ ,

$$|f_x| = |\lambda - \lambda_o|/d\lambda = |\lambda - \lambda_o| * R/\lambda \approx (2W_x/\lambda) \sin \gamma \cos \theta.$$

Hence, the interferogram consists of spatial fringe frequencies heterodyned with respect to  $\lambda_o$ . The wavelength  $\lambda_o$  is an imposed reference that typically corresponds to the center of the target bandpass and is referred to as the tune of the interferometer. The use of rotating optical components to align the interferometer allows it to be tuned to any wavelength defined by the diffraction grating and other physical constraints of the instrument. The FLP is recorded on a detector and then Fourier transformed to recover the input spectrum.

In addition to this wavelength-dependent angular separation of the wavefronts  $\gamma$ , a rotation ( $\phi$ ) can be introduced perpendicular to the diffraction plane through a small tilt in the “pilot-flat” mirror. The effect is a counter-rotation of the wavefronts, manifested as a vertical fringe frequency [ $f_y = (2W_y/\lambda) \sin \phi$ ] in the interference pattern (Fig. 9 bottom). Although there is no wavelength dependence on the magnitude

of  $\phi$  (nonheterodyned), the direction of fringe rotation (clockwise, CW versus counter-clockwise, CCW) is now dependent on the sign of  $\lambda - \lambda_o$ , thus breaking the symmetry of  $|\lambda - \lambda_o|$ . This eliminates aliasing and is observed as a  $\pm$  vertical separation of degenerate wavelength components in the power spectrum of a 2D Fourier transform of the pattern (Fig. 10). For unknown sources, this effect can provide an overall increase in accuracy of the spectral data in both wavelength and intensity while essentially doubling the usable (nondegenerate) bandpass. Further, it produces a separation of the target spectral components from any undesired zero-zero signal common in the center of the 2D power spectrum (Fig. 10), a notable improvement over previous all-reflective designs (e.g., [3,18]).

There are some factors that influence the wavelength accuracy and the achieved resolving power that can become considerable when attempting to sample relatively large wavelength ranges. It is evident from the equations for  $f_x$  and  $R$  that the wavelength scale is not purely linear. The theoretical resolving power ( $R_{\text{Theor}} = \lambda/d\lambda = 4 \text{ mW}/d$ ) is constant and also wavelength independent; thus as the wavelength interval sampled changes the spectral dispersion also changes. Other factors

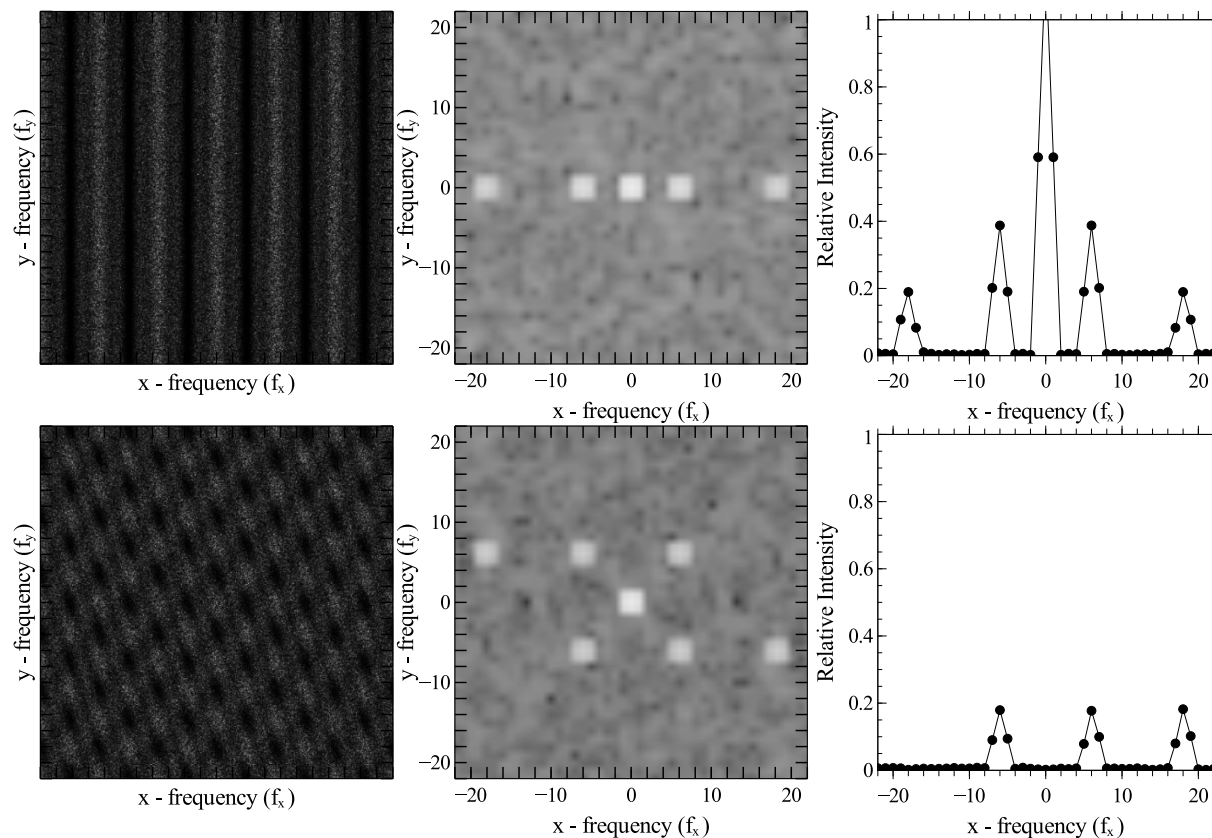


**Fig. 10.** Dealiasing: Input contains three equal intensity monochromatic wavelengths corresponding to  $x$  frequencies  $-6$ ,  $6$ , and  $18$ . From left to right: 2D interferograms, associated power spectra, and the fast Fourier transform (FFT) output spectra. Top: No  $y$  tilt. The spectrum in the top-right is from  $f_y = 0$ . Bottom:  $y$  tilt corresponding to a  $y$  frequency separation of  $-6$  (and  $6$ ); the full accurate spectrum is shown on the bottom right, obtained from  $f_y = -6$ . The spectrum from  $f_y = 6$  (not shown) is a transposed mirror of the information in  $f_y = -6$  (i.e., identical spectrum but with wavelength decreasing from left to right). The interferograms are produced through Zemax.

(e.g., the projected and effective area of interference on the sensor to be transformed) likewise become increasingly apparent the further from  $\lambda_0$  sampled. These considerations have the potential to also produce line broadening, thus reducing the achieved resolving power. FOV effects can also play a role in a similar manner: For example, a monochromatic point source will be broader than a monochromatic aperture filling source, and a point source from the edge of the FOV could also experience detectable line broadening compared to a point source centered in the input aperture. A formal treatment of these factors is out of the scope of this report and will be addressed in future studies, but an interested reader can find some discussion in [2]. Importantly, all of these considerations are negligible in the narrowband ARC-SHS data discussed in this report (Figs. 4–6 and Table 1).

**Funding.** National Aeronautics and Space Administration (NASA) (NAG5-12812, NNG05WC22G, NNX07AU10G).

**Acknowledgment.** We are thankful to the staff at McMath–Pierce solar telescope on Kitt Peak for their support and to John Harlander for the many insightful discussions he has provided.

## REFERENCES

1. I. R. Abel, B. R. Reynolds, J. B. Breckinridge, and J. Pritchard, "Optical design of the ATMOS Fourier transform spectrometer," *Proc. SPIE* **193**, 12–26 (1979).
2. J. M. Harlander, "Spatial heterodyne spectroscopy: interferometric performance at any wavelength without scanning," Ph.D. dissertation (University of Wisconsin, 1991).
3. S. Chakrabarti, D. Cotton, J. Vickers, and B. Bush, "Self-compensating, all-reflection interferometer," *Appl. Opt.* **33**, 2596–2607 (1994).
4. W. M. Harris, F. L. Roesler, J. Harlander, L. Ben-Jaffel, E. Mierkiewicz, J. Corliss, and R. J. Oliverson, "Applications of reflective spatial heterodyne spectroscopy to UV exploration in the solar system," *Proc. SPIE* **5488**, 886–897 (2004).
5. J. B. Corliss, "Large-field high resolution spectroscopy: Development of all-reflective spatial heterodyne spectrometers and astronomical results using an image slicer from the McMath–Pierce main spectrograph," Ph.D. dissertation (University of Wisconsin, 2011).
6. Y. Bétrémieux, J. Corliss, M. B. Vincent, F. E. Vincent, F. L. Roesler, and W. M. Harris, "Description and ray-tracing simulations of HYPE: a far-ultraviolet polarimetric spatial-heterodyne spectrometer," *Proc. SPIE* **7732**, 77322C (2010).
7. W. M. Harris and J. B. Corliss, "Performance and validation of a sub-orbital FUV spatial heterodyne spectro-polarimeter optimized for wide-field observations of interplanetary hydrogen," *Proc. SPIE* **9144**, 91442Y (2014).



8. O. R. Dawson and W. M. Harris, "Tunable, all-reflective spatial heterodyne spectrometer for broadband spectral line studies in the visible and near-ultraviolet," *Appl. Opt.* **48**, 4227–4238 (2009).
9. J. M. Harlander, J. E. Lawler, J. Corliss, F. L. Roesler, and W. M. Harris, "First results from an all-reflection spatial heterodyne spectrometer with broad spectral coverage," *Opt. Express* **18**, 6205–6210 (2010).
10. J. B. Corliss, W. M. Harris, F. L. Roesler, E. J. Mierkiewicz, and R. J. Oliverson, "High resolution spectroscopy of Comet 9P/Tempel 1 before and after the deep impact event: evidence for anomalous emission near the 630 nm [O('D)] emission line," in preparation.
11. W. M. Harris, J. B. Corliss, J. Bobula, and R. A. Diaz-silva, "HYPE: performance and validation of a suborbital FUV spatial heterodyne spectro-polarimeter," in preparation.
12. C. R. Englert and J. M. Harlander, "Flatfielding in spatial heterodyne spectroscopy," *Appl. Opt.* **45**, 4583–4590 (2006).
13. C. E. Moore, M. G. J. Minnaert, and J. Houtgast, *The Solar Spectrum 2935 Å to 8770 Å* (U.S. Government Printing Office, 1966).
14. C. B. Markwardt, "Non-linear least-squares fitting in IDL with MPFIT," in *Astronomical Data Analysis Software and Systems XVII*, D. A. Bohlender, D. Durand, and P. Dowler, eds., Vol. **411** of *Astronomical Society of the Pacific Conference Series* (2009), pp. 251–254.
15. J. H. Woodman, W. D. Cochran, and D. B. Slavsky, "Spatially resolved reflectivities of Jupiter during the 1976 opposition," *Icarus* **37**, 73–83 (1979).
16. C. R. Benn and S. L. Ellison, "Brightness of the night sky over La Palma," *New Astron. Rev.* **42**, 503–507 (1998).
17. S. K. Midya and S. N. Ghosh, "Seasonal variations of OI 6300 Å night airglow emission at Calcutta and other stations and its covariation with OI 5577 Å emission," *Earth Moon, Planets* **66**, 145–152 (1994).
18. S. G. Stephan, S. Chakrabarti, J. Vickers, T. Cook, and D. Cotton, "Interplanetary H Ly  $\alpha$  observations from a sounding rocket," *Astrophys. J.* **559**, 491–500 (2001).